Geophys. J. Int. (2002) **148,** 278–287

Convection-driven motion of the North American craton: Evidence from *P*-wave anisotropy

Götz H. R. Bokelmann

Department of Geophysics, Stanford University, Stanford, CA 94305-2215. E-mail: goetz@pangea.stanford.edu

Accepted 2001 October 3. Received 2001 October 1; in original form 2000 December 4

SUMMARY

We study the effect of anisotropy on *P*-wave traveltimes and generalize Backus (1965) well-known expression of azimuthal velocity dependence to the sphere. The variation of *P*-wave traveltimes on the lower hemisphere due to anisotropy is described by a set of 15 parameters. For single-crystal olivine a set of six parameters describes about 98 per cent of the variation and for practical purposes of mantle seismology this set of six parameters should be sufficient. We find a coherent pattern of anisotropy throughout the North American craton. The anisotropy is characterized by fast directions dipping toward the southwest, roughly in the direction of absolute plate motion, and shallow dip angles ($<45^\circ$). This is consistent with a simple-shear deformation of the deep lithospheric roots, due to the relative motion between plates and deeper mantle. If this is correct, it implies that the deeper mantle convects faster than the plate velocity and that the mantle helps to drive the motion of the North American plate.

Key words: anisotropy, lithosphere, lithospheric deformation, mantle convection, plate tectonics, traveltime.

1 INTRODUCTION

It is well-established that continents can move relative to each other (Hess 1964), and the current relative motions are reasonably well-determined from VLBI, satellite geodesy and geological data (Larson *et al.* 1997). It is less well-known, however, how this motion is accommodated at depth, and also the question of which forces drive the motion is open and under current debate. Here we propose that important insight can be gained by considering the deformation in the continental lithosphere and especially in the deep lithospheric roots. Tomographic models (Zhang & Tanimoto 1990; Grand 1994) and the reduced heat flow at the surface (Pollack *et al.* 1993) have shown that these thick lithospheric roots generally underly the Precambrian Shields and they seem to be up to 400 km thick (Polet & Anderson 1993) raising the question how shields can move if they are deeply indented into the mantle. It is important in this context that several of the shields are known to be associated with strong anisotropy which indicates a strong degree of internal deformation. This is especially the case for the Canadian Shield (Bokelmann & Silver 2000), which is one of the very thickest shields. Previous inversions for the anisotropy of the Canadian Shield required the presence of two anisotropic layers to fit shear-wave splitting observations together with *P*- and *S*-wave station delays. These inversions required the deeper layer to have subhorizontal foliation and strong anisotropy, which is consistent with a mechanical interaction with the deeper mantle. The strong anisotropy also indicates that teleseismic *P*-wave travel delays (traveltimes minus traveltimes predicted from a reference earth model) should vary with the direction of arrival by 2 s or more under the Canadian shield. In this study we use observations of *P*-wave delays from stations in North America to test this prediction and to study the directional dependence of *P*-wave velocities.

The directional dependence of *P*-wave delays may in principle determine the dip angle of the fast direction, in addition to its azimuth. The former quantity is usually not resolved from shear-wave splitting (and anisotropic surface-wave tomography). On the other hand, shear-wave splitting has the advantageous property that it is virtually unaffected by lateral heterogeneity. This is different for *P*-wave traveltimes, and we need to address the trade-off between anisotropy and lateral heterogeneity. In light of this trade-off, previous studies dealing with traveltimes considered either anisotropy or lateral heterogeneity and essentially ignored the other. It is becoming increasingly clear that we are dealing with both heterogeneity and anisotropy in the Earth and that they may often have equally strong effect on the data. But different from heterogeneity, the effect of anisotropy on *P*-wave delays can take only certain geometrical shapes on the lower hemisphere. Therefore the approach taken in this paper is to first consider delay variation, which may arise from anisotropy under North America, and to later on discuss possible effects of lateral heterogeneity.

Seismic anisotropy is an important tool for understanding the mode of deformation in the mantle and its geometry. There are a number of important questions, which motivate a detailed study of anisotropy under the Canadian Shield. Is the anisotropy frozen-in as fossil deformation or is it due to current deformation? At which depth does the dislocation-creep indicated by anisotropy occur? Is

there a mechanical asthenosphere under the continental lithosphere and how strong is the coupling of continental plates with the deeper mantle? Do plates drive the convective flow in the upper mantle or does mantle convection help to drive plate motion? Our inferences about the deep Canadian Shield from *P*-wave delays, especially the dip angle of anisotropic axes, will allow addressing these questions.

2 WEAK ANISOTROPY

Linear plane wave propagation is governed by the eigenvalue problem

$$m_{jk}a_k = v^2 a_j \tag{1}$$

with $m_{jk} = c_{jkmn}\hat{x}_m\hat{x}_n/\rho$ and phase velocity v, polarization $\mathbf{a}$, density ρ, and the elasticity tensor c_{ijkl}. $\hat{\mathbf{x}}$ is the wavefront normal direction. It is convenient to write the elasticity tensor as a small perturbation $\delta\Gamma_{ijkl}$ from a reference state Γ_{ijkl}, that is $c_{ijkl} = \Gamma_{ijkl} + \delta\Gamma_{ijkl}$. Backus (1965) showed that the *P*-wave velocity variation can be described as

$$\delta v_p = \frac{1}{2\rho v_p^0}\delta\Gamma_{ijkl}\hat{x}_i\hat{x}_j\hat{x}_k\hat{x}_l \tag{2}$$

with the isotropic reference velocity v_p^0. (2) is a 4th-order polynomial in $\hat{\mathbf{x}}$. For the 2-D case of propagation in a horizontal plane Backus (1965) showed that the polynomial (in azimuth θ) takes the form

$$\delta v_p = \sum_{n=0}^{4} A_n \cos^n\theta \sin^{4-n}\theta \tag{3}$$

which can be rearranged into the form of a Fourier series

$$\delta v_p = A + C\cos 2\theta + D\sin 2\theta + E\cos 4\theta + F\sin 4\theta \tag{4}$$

Thus 5 parameters describe the variation of the *P*-wave velocity in the horizontal plane, and they are related to the elastic coefficients as

$$\begin{aligned}
8A &= 3\delta\Gamma_{1111} + 2\delta\Gamma_{1122} + 4\delta\Gamma_{1212} + 3\delta\Gamma_{2222}\\
2C &= \delta\Gamma_{1111} - \delta\Gamma_{2222}\\
D &= \delta\Gamma_{1112} + \delta\Gamma_{1222}\\
8E &= \delta\Gamma_{1111} - 2\delta\Gamma_{1122} - 4\delta\Gamma_{1212} + \delta\Gamma_{2222}\\
2F &= \delta\Gamma_{1112} - \delta\Gamma_{1222}
\end{aligned} \tag{5}$$

The 3-D case has been discussed by Backus (1970), Sayers (1994) and Mochizuki (1995) using spherical harmonic expansions of the angular velocity variation. Backus (1970) showed that the *P*-wave velocity variation δv_p depends only on S_{ijkl}, the totally symmetric part of $\delta\Gamma_{ijkl}$

$$S_{ijkl} = \frac{1}{3}(\delta\Gamma_{ijkl} + \delta\Gamma_{ikjl} + \delta\Gamma_{iljk}) \tag{6}$$

and that the *P*-velocities uniquely specify S_{ijkl}, which has at most 15 independent parameters. The antisymetric part, A_{ijkl}, with

$$A_{ijkl} = \delta\Gamma_{ijkl} - S_{ijkl} \tag{7}$$

can not be determined from *P*-wave velocities. From the orthonormal expansion we may obtain a Fourier expansion in terms of trigonometric functions of azimuth θ and incidence angle ϕ. Appendix A shows that the velocity variation on the sphere takes the form

$$\begin{aligned}
\delta v_p \approx\ & A + B\cos 2\phi + C\cos 2\theta + D\sin 2\theta + G\sin 2\phi\cos\theta\\
& + H\sin 2\phi\sin\theta + J\cos 2\phi\cos 2\theta + K\cos 2\phi\sin 2\theta
\end{aligned} \tag{8}$$

where higher angular degrees and/or orders than 2 are omitted. Eq. (8) can be represented as a second-order polynomial

$$\delta v_p = G_{ij}\hat{x}_i\hat{x}_j \tag{9}$$

and we can identify its coefficients as

$$\begin{aligned}
A &= \frac{1}{4}(G_{11} + G_{22} + 3G_{33})\\
B &= \frac{1}{4}(-G_{11} - G_{22} + 2G_{33})\\
C &= \frac{1}{4}(G_{12} - G_{22})\\
D &= \frac{1}{4}G_{12}\\
G &= G_{13}\\
H &= G_{23}\\
J &= \frac{1}{4}(-G_{11} + G_{22})\\
K &= -\frac{1}{2}G_{12}
\end{aligned} \tag{10}$$

Although eq. (8) contains 8 unknowns, only 6 of these are linearly independent. Sayers (1994) studied the nature of the velocity variation and showed that for steep incidence angles the *P*-wave velocity varies with angle as $\cos 2\theta$. Indeed, it is customary to include only terms up to degree and order 2 (Mochizuki 1995), since higher-order terms are usually hard to resolve with teleseismic data. This would reduce the number of independent parameters to 6. Further motivation for considering only variation up to order and degree 2 follows from single-crystal olivine, which is the major constituent of mantle anisotropy (Nicolas & Christensen 1987). Olivine has orthorhombic symmetry, and its elastic coefficients c_{ijkl} are given by Kumazawa & Anderson (1969). Fig. 1 gives the ray geometry in the upper mantle and the angular delay pattern (lower hemisphere) for an olivine 'crystal' with an a-axis dipping 30° in Southwestern direction (from the horizontal). The (intermediate) c-axis is horizontal and the slow b-axis dips in Northeastern direction. These delays were computed using eq. (2) and the elastic constants from Kumazawa & Anderson (1969). However, a delay pattern predicted using the second-order polynomial (9) instead of the fourth-order polynomial

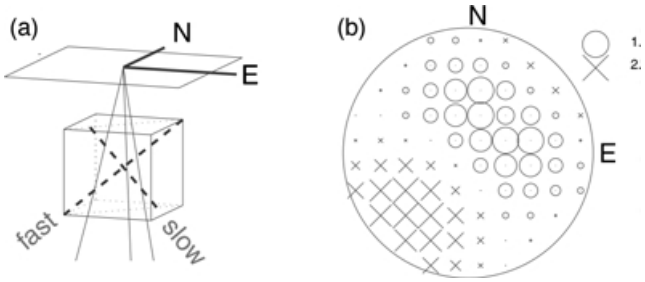

Figure 1. (a) Ray geometry in the upper mantle computed using the PREM velocity model (Dziewonski & Anderson 1981) illustrating that teleseismic rays propagate on nearly straight ray paths in the upper mantle (shown from the surface to 300 km depth). An anisotropic block of olivine causes a direction-dependence of *P*-wave delays. The 'single crystal' has a fast a-axis dipping 30° to the Southwest, a slow b-axis dipping 60° to the Northeast, and a horizontal c-axis. The lower hemisphere in (b) shows predicted fast/slow delays (crosses, circles respectively) from propagation through the 150 km thick layer (given in seconds).

is virtually indistinguishable from Fig. 1(b). The quadratic misfit is only about 2 per cent suggesting that the second-order polynomial gives a reasonably good description of the velocity variation and that the real traveltime observations probably don't require inclusion of the higher-order terms.

3 INVERTING FOR ANISOTROPY

Delay times dt are obtained from a given G_{ij} through integration along the ray paths L

$$dt = \int_L \frac{ds}{v(\mathbf{r})} - \int_{L_0} \frac{ds}{v^0(\mathbf{r})} \tag{11}$$

This equation is weakly nonlinear, and it becomes linear if we assume that the traveltimes can be computed by integration along the known reference ray path L_0. This assumption holds to first order (Nolet 1987).

$$dt \approx -\int_{L_0} \frac{\delta v(\mathbf{r})}{v_P^2(\mathbf{r})}\, ds = -\int_{L_0} \frac{G_{ij}(\mathbf{r})\hat{x}_i\hat{x}_j}{v_P^2(\mathbf{r})}\, ds \tag{12}$$

with the ray direction $\hat{\mathbf{x}}(\mathbf{r}) = |d\mathbf{r}/ds|$ along the ray.

Based on the observation that anisotropy is localized in the depth region shallower than 400 km depth (Montagner 1996) we will assume in the following that the anisotropic properties of the mantle under each station can be described by a single anisotropic layer in the upper mantle which has constant anisotropic properties. We will show later that this assumption is justified even if there are multiple anisotropic layers in the upper mantle because they can not be distinguished using teleseismic data due to the nearly straight ray paths apparent from Fig. 1(a). We are then dealing with the linear inverse problem

$$dt = \left(-\int_{L_0} \frac{\hat{x}_i\hat{x}_j}{v_P^2(z)}\, ds \right) G_{ij} \tag{13}$$

where we assume a purely depth-dependent (1-D) reference model. In the following we will solve this linear inverse problem

$$\mathbf{d} = \mathbf{Am} \tag{14}$$

with data $\mathbf{d} = (dt_1, dt_2, \ldots, dt_N)^T$, matrix $\mathbf{A}$, and model parameters

$$\mathbf{m} = (G_{11}, G_{22}, G_{33}, G_{12}, G_{13}, G_{23})^T. \tag{15}$$

Eigenvectors $\hat{\mathbf{e}}_1, \hat{\mathbf{e}}_2, \hat{\mathbf{e}}_3$ of the coefficient matrix

$$\mathbf{G} = \begin{pmatrix} G_{11} & G_{12} & G_{13} \\ G_{12} & G_{22} & G_{23} \\ G_{13} & G_{23} & G_{33} \end{pmatrix} = \mathbf{ELE}^T = \sum_i \hat{\mathbf{e}}_i l_i \hat{\mathbf{e}}_i^T, \tag{16}$$

give the directions of fastest, intermediate and slowest average velocity along the ray path with the eigenvalues l_1, l_2, and l_3 giving the associated velocity perturbations. Respectively the earliest, intermediate, and latest arrival times are cl_1, cl_2, and cl_3 with $c = -L^2/(|\hat{x}_3|\bar{v}_P^2)$. For a spherical shell around the station $L^2/(|\hat{x}_3|)$ is replaced by L.

4 DATA

In the following we will study anisotropic effects in arrival time data for stations on and around the Canadian Shield. There are about 20 stations in the area of the shield that contributed more than 1000 P-wave arrival times to the International Seismological Center (ISC) between 1964 and 1999. These stations are typically separated by several hundred kilometres. The events in this study have been relocated (Engdahl *et al.* 1998; Kárason & Van der Hilst 2001) to remove source mislocation biases on traveltime residuals. The traveltime residuals (relative to the AK135 reference model Kennett, Engdahl & Buland 1995) are shown for an example station in Fig. 2 (histograms). A logarithmic display reveals long tails of the distribution, which are probably due to mispicks. For small residuals these mispicks are buried among the correctly picked arrival times, but at large residual they stand out and can be removed without corrupting the data set. We use a threshold of ± 3 s and eliminate larger residuals from the inversion.

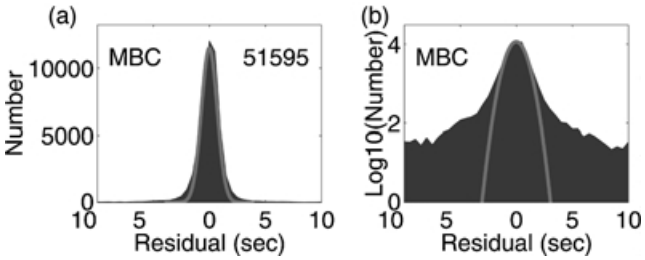

Figure 2. Histogram of the 51595 residuals of station MBC around the mean, shown a) linearly, b) logarithmically. The changing slope near ± 3 s suggests that most of the larger residuals are spurious and should not be used in the inversion. For illustration a Gaussian distribution curve is overlain ($\sigma = 1$ s).

5 RESULTS

Fig. 3(a) shows the distribution of data points for one station on the Canadian Shield, RSON (Red Lake, Ontario), and averaged residuals on the lower hemisphere. For stations remote from seismogenic areas such as RSON there are few rays with shallow incidence angle. In fact, for RSON almost all rays are in a range from 0° (vertical) to 60°. The general similarity (fast west, slow northeast) of the residual pattern in Fig. 3(b) and the synthetic data for olivine (Fig. 1b) suggests that the fast axis $\hat{\mathbf{e}}_1$ under RSON is dipping to the southwest as well. In the following we will present inversion results for RSON and we will start with a discussion of the sensitivity of the inversion with respect to the starting model. Fig. 4 shows the traveltimes predicted from the best-fitting model. These predictions are again similar to Fig. 1(b), except that the slow orientation is not subvertical but has an intermediate angle between vertical and 'transverse'

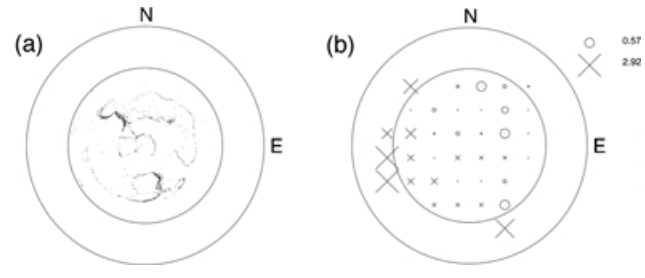

Figure 3. (a) Data distribution on the lower hemisphere for station RSON (5196 data points). The incidence angle $\phi = \sin^{-1}(pv_p)$ of rays from the vertical is given for a depth of 200 km ($v_p = 8.5$ km s^{-1}, p = ray parameter). (b) shows the data averaged onto a 80 cell regular grid (display similar to Fig. 1b). The circles correspond to incidence angles of 55° and 90° from the vertical. Note that the data distribution is good for incidence angles steeper than 55° (the few blocks for shallower incidence are constrained by only few data points).

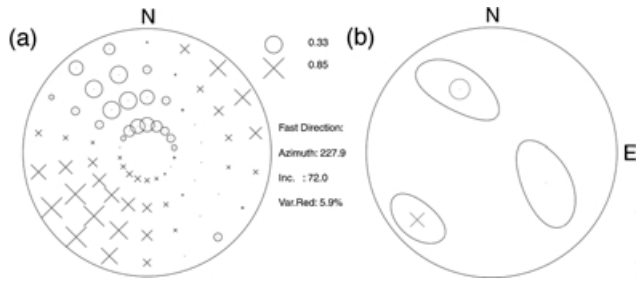

Figure 4. (a) Traveltime variation associated with the best-fitting model G_{ij} (eq. 13). (b) Confidence regions of the axes orientations (for 1 σ). The fast direction is given by a cross, the slow direction by a circle (see text).

horizontal. Also the confidence regions for the slow and intermediate directions (see Fig. 4b) are elongated around the fast direction suggesting that the fast direction $\hat{\mathbf{e}}_1$ is better-determined than $\hat{\mathbf{e}}_2$ and $\hat{\mathbf{e}}_3$. The fast azimuth is 227.9° and the incidence angle (from the vertical) is 72°. The predicted delays range from −0.85 to 0.33 s, and are thus about a third of the range in the averaged data (Fig. 3b). The variance reduction in this example is 5.9 per cent and for other stations in this paper they range between 1 and 20 per cent.

Fig. 5 shows fast directions for a representative set of stations (also see the results in Table 1) including all stations in the shield area (Eastern Canada) which provided more than 1000 arrival time data. It has been noted before that the area of anomalously fast mantle (map background) and the spatial extent of the geologically stable craton agree quite well (Grand 1994). This is usually explained by the existence of a particularly thick lithosphere under that region. In the following we will regard fast mantle with upper-mantle shear-wave delay $dt_S < -2$ s from the model of Grand (1994) as indicating that thick lithospheric root under the craton. 11 out of 12 stations on this root are also located on or at the edge of the shield. Note that all stations (origin of arrows) which are located on thick root consistently have Southwestern fast directions (black color), whereas such fast directions are very rare among the stations off the shield root (light gray background). Generally, there is good spatial consistency in fast directions between neighbouring stations. The strong change in fast direction at the edge of the craton suggests that there are no effects from left-over source mislocation but that the variation is due to properties of the lithosphere.

We will now further address the question of stability of the results and in particular, the effect of the limited range in incidence angles apparent in Fig. 3. Fig. 6 uses the olivine example from Fig. 1(b) to test the influence of restricting the range of incidence angles and to simulate the observation geometry. In the noise-free case (Figs 6b and c) uncertainties for the restricted and the full data set are quite similar. In both cases the fast direction is much better resolved than $\hat{\mathbf{e}}_2$ and $\hat{\mathbf{e}}_3$. This is due to the fact that the velocities along the b- and c-axes (7.72 km s^{-1}, 8.43 km s^{-1}) differ much less than between them and the a-axis (9.89 km s^{-1}). The same occurred in the data inversion (see Fig. 4). Fig. 6(d) tests the restricted case with an added noise variance equal to the variance in the traveltime predictions of Fig. 6(a). Resolution of $\hat{\mathbf{e}}_2$ and $\hat{\mathbf{e}}_3$ becomes difficult, but the fast axis $\hat{\mathbf{e}}_1$ is well-resolved. In principle the same occurs in the case of a horizontal a-axis (Fig. 7). It is somewhat harder to resolve $\hat{\mathbf{e}}_2$ and $\hat{\mathbf{e}}_3$ in the noisy case, but $\hat{\mathbf{e}}_1$ is again well-resolved. This is an important test. It indicates that we can resolve the orientation of the fast axis, and that the fast axes for the region of the craton (Fig. 5) are really dipping in the southwestern and not in the northeastern direction.

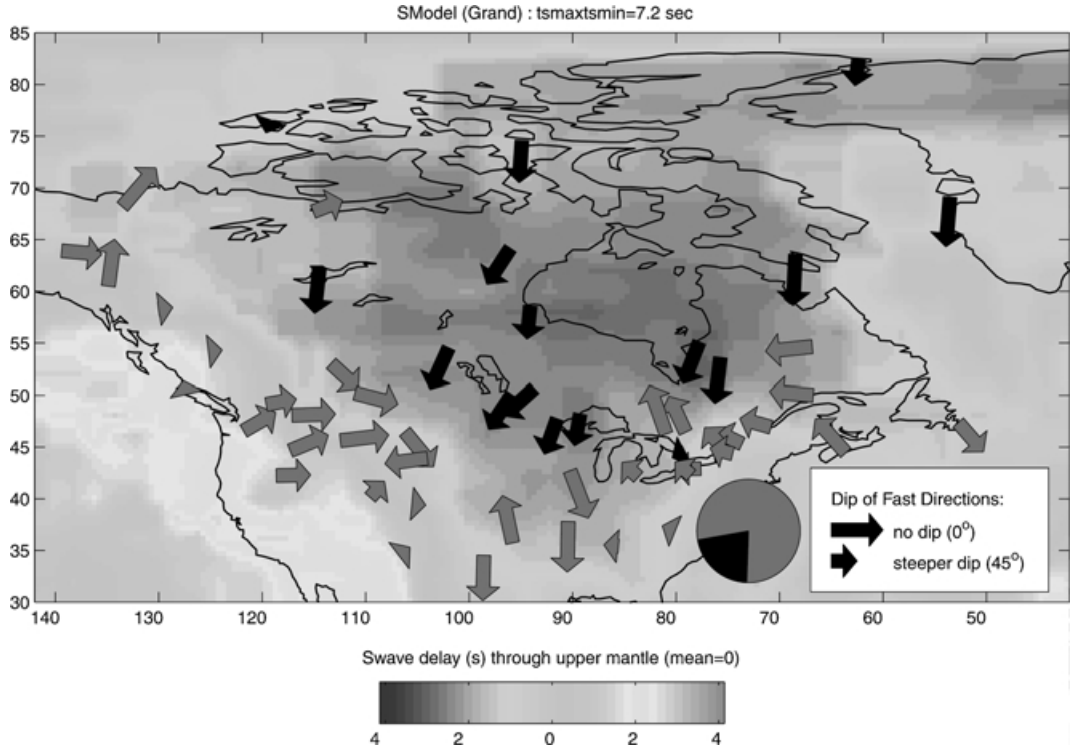

Figure 5. Orientations of fast axes for stations in North America. Azimuths between 180° and 260° are shown in black, others in gray. These azimuthal ranges are illustrated in the 'pie chart'. The background shows the vertically integrated traveltime residuals dt_S through the upper mantle in the tomographic *S*-wave model of Grand (1994) with the mean removed. Note that stations on fast mantle (dark colours, stable North American craton) show southern to southwestern fast directions whereas stations off the craton show very different fast directions. The length of the lines shows the dip angle from the horizontal.

Table 1. Fast directions for stations in this study.

Station	Latitude	Longitude	Fast azimuth[1]	Fast dip[2]	VarRed.[3]
AAM	42.11	−83.66	312 (148–42)	52 (−22–82)	2
ALE	82.45	−62.35	188 (179–197)	43 (34–52)	12
ALQ	34.76	−106.46	52 (266–78)	73 (41–90)	1
BLA	37.02	−80.42	292 (257–316)	72 (62–82)	10
BLC	64.17	−96.02	213 (203–223)	15 (8–22)	7
BMO	44.66	−117.31	68 (61–74)	18 (14–23)	7
CMC	67.70	−115.08	68 (37–112)	35 (4–64)	1
CPO	35.41	−85.57	275 (235–308)	64 (54–73)	5
DAWY	63.91	−139.39	95 (53–134)	20 (7–30)	4
DLBC	58.27	−130.03	82 (47–209)	65 (25–88)	5
EDM	53.04	−113.35	133 (123–142)	26 (23–28)	16
EEO	46.45	−79.07	335 (286–17)	21 (−2–42)	4
EYMN	47.75	−91.50	200 (155–249)	24 (2–45)	9
FBX	63.58	−68.47	183 (171–195)	0 (−5–6)	3
FCC	58.59	−94.09	186 (169–206)	32 (11–52)	4
FFC	54.54	−101.98	204 (183–225)	11 (2–19)	6
FSJ	54.28	−124.28	83 (10–131)	83 (76–90)	14
FVM	37.80	−90.43	181 (171–192)	2 (−3–7)	9
FYU	66.42	−145.23	156 (59–220)	75 (30–80)	17
GDH	69.12	−53.53	185 (170–200)	3 (−5–11)	2
GOL	39.51	−105.37	96 (77–110)	69 (62–75)	5
GWC	55.11	−77.75	201 (182–221)	12 (−3–27)	5
HAL	44.44	−63.59	318 (291–349)	10 (−13–33)	6
INK	68.17	−133.52	41 (38–43)	0 (−2–3)	12
JAQ	53.62	−75.72	187 (161–215)	10 (−11–29)	12
JFWS	42.72	−90.25	159 (123–195)	1 (−21–23)	4
LAO	46.50	−106.22	141 (130–151)	11 (7–15)	6
LHC	48.23	−89.27	190 (168–219)	33 (13–52)	7
LON	46.56	−121.81	60 (53–68)	25 (10–40)	11
LRM	45.63	−112.45	83 (70–96)	5 (−4–15)	1
MBC	76.15	−119.36	199 (189–209)	74 (66–82)	3
MNT	45.31	−73.62	296 (286–305)	40 (31–48)	20
NEW	48.07	−117.12	88 (82–95)	15 (9–20)	8
OTT	45.20	−75.72	318 (301–330)	49 (35–62)	16
PHC	50.52	−127.43	348 (321–57)	74 (60–86)	10
PNT	49.13	−119.62	80 (61–88)	37 (−4–77)	3
RES	74.59	−94.90	184 (173–195)	16 (11–22)	7
ROC	42.93	−77.59	269 (92–88)	44 (−15–79)	3
RSNY	44.35	−74.53	285 (263–304)	49 (37–62)	13
RSON	50.67	−93.70	228 (209–246)	18 (5–31)	6
RSSD	43.93	−104.04	262 (250–275)	15 (−2–32)	4
SADO	44.58	−79.14	244 (65–51)	65 (31–88)	4
SCHQ	54.65	−66.83	264 (252–277)	8 (1–15)	4
SES	50.21	−111.04	105 (90–119)	13 (−9–35)	1
SFA	46.93	−70.83	285 (265–309)	34 (9–58)	14
SIC	49.98	−66.74	275 (247–305)	14 (−9–36)	4
STJ	47.38	−52.73	139 (105–175)	23 (4–41)	6
SUD	46.27	−80.97	341 (322–360)	1 (−18–20)	15
TUL	35.73	−95.79	348 (337–359)	6 (2–9)	4
UBO	40.13	−109.57	41 (23–67)	52 (32–72)	3
ULM	50.06	−95.88	214 (175–250)	17 (−3–37)	3
WHY	60.49	−134.88	8 (345–31)	8 (−17–32)	7
WMO	34.54	−98.59	181 (141–220)	11 (−2–23)	7
WVOR	42.24	−118.64	89 (66–142)	30 (−16–72)	3
YKX	62.32	−114.47	186 (130–238)	9 (−10–21)	5
YSNY	42.28	−78.54	310 (134–124)	53 (3–86)	4

[1]Measured from north to east. Confidence regions are given in brackets.
[2]Measured from the horizontal downwards. Confidence regions are given in brackets.
[3]Variance reduction in per cent.
[4]FBX is a composite of the nearby stations FRB and FBC. Similarly, YKX consists of stations YKA, RSNT, and YKC.

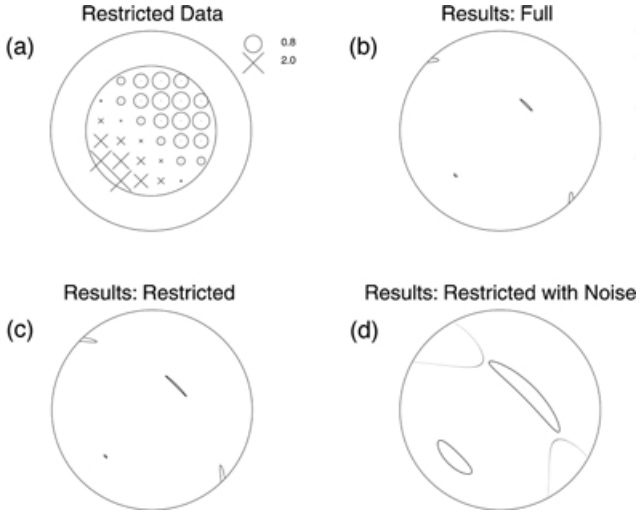

Figure 6. Test of the effect of a restricted data distribution. From the synthetic model in Fig. 1(b) (olivine with fast axis dipping 30° in SW-direction) we choose a restricted subset with incidence angles between 0° and 50° from vertical (a). Circles are drawn at 90° and 55° from vertical. (b) and (c) show resulting confidence regions (1σ) for the full and the restricted data set, in a fashion similar to Fig. 4. (d) shows results for the restricted data set with added random uncorrelated time fluctuations to mimic the noise conditions in the observations (see text).

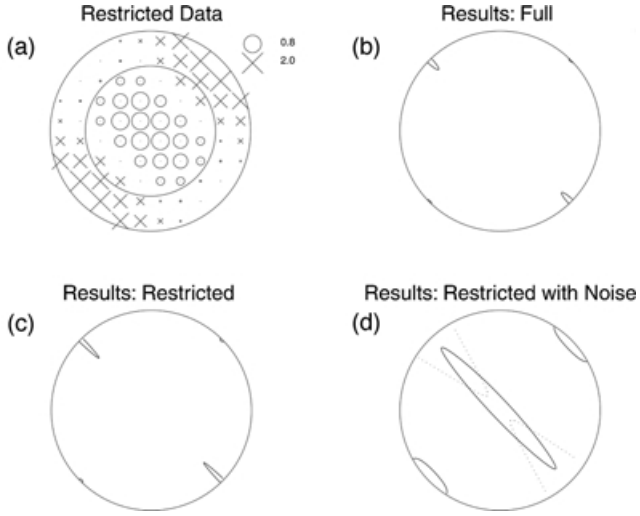

Figure 7. Effect of a restricted data distribution for a horizontal/vertical orientation of principle axes (olivine fast axis in SW direction, dip 0°). Otherwise as in Fig. 6.

Variance reductions are typically above 98 per cent for (b) and (c) and about 55 per cent for (d).

6 FAST DIRECTION ORIENTATIONS

To better understand the cause of the coherent anisotropy of the Canadian Shield, Fig. 8 shows the azimuthal distribution of fast directions for the stations in Fig. 5. The stations on the craton (fast mantle with delay $dt_S < -2$ s) have azimuths between 180° and 260°, which fall in the range of directions of absolute plate motions in the area. Such a general agreement between fast axes and absolute plate motion directions has been noted before, for fast axes from SKS-shear-wave splitting (Vinnik *et al.* 1992). However, geological

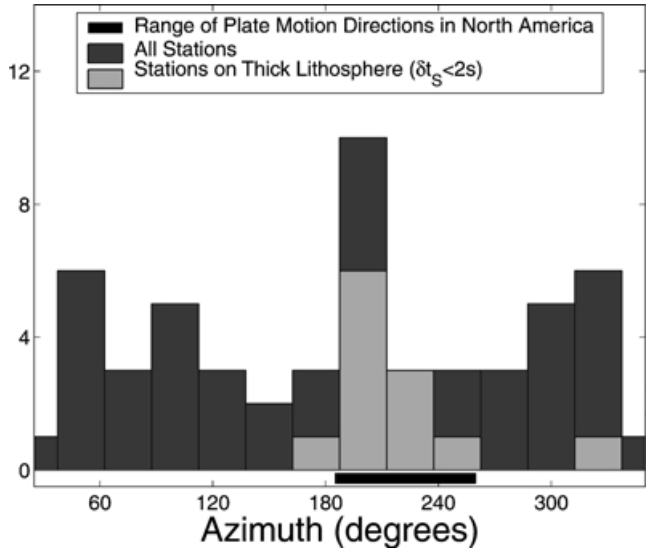

Figure 8. Histogram of fast direction azimuths. Values for stations on thick lithosphere ($dt_S < -2$ s, the craton) are shown in light gray, and the histogram for all data is given in dark grey. Values from the craton agree well with the range of absolute plate motion directions in North American (model by Gripp & Gordon 1990).

foliation orientations have often roughly similar orientation, and seem to fit the data as well or even better (Silver & Chan 1991). Azimuthal information alone may not allow distinguishing these two possible causes of anisotropy in North America, namely fossil deformation and deformation from plate–mantle interaction (PMI). But a constraint is given by the dip angle of the fast axes because the effect of a finite simple shear on an initially isotropic lithosphere is to rotate mineral grains into a preferred orientation. Wenk *et al.* (1991) showed that an olivine polycrystal assumes a preferred orientation of b-axes (normal to the weakest planes) that forms an angle Θ with the (horizontal) shear plane, which is

$$\tan 2\Theta = \frac{2}{\gamma} \tag{17}$$

depending on the level of simple-shear strain γ. Clearly, Θ is never larger than 45° and it approaches 0° for large strains. Thus the model of simple-shear predicts dip angles on the thick root to be shallower than 45°. Fig. 9 indeed shows that all 12 measurements on the craton (delays $dt_S < -2$ s) satisfy this test. Their dip angles are shallower than 45° (measured from the horizontal). For slower mantle only 65 per cent of the stations have incidence angles shallower than 45° (29 out of 44).

An interpretation of the coherent anisotropy of the lithospheric root is given in Fig. 10. Relative motion between lithosphere and deeper mantle may cause simple-shear deformation in the lithospheric root under the craton. If this interpretation is correct, then the azimuths in positive plate motion direction imply that the deeper mantle helps to drive plate motion. The mantle motion is parallel to and faster than the plate motion under North America. But note that we infer this mechanism only for the region of thick lithosphere, the craton. Other regions may experience effects from flow around the keel and may therefore show more complex anisotropy. In the region of the keel we also expect increased mechanical interaction, that is higher stresses in the upper mantle. Therefore the motion under this region influences North American plate motion more than in other regions. An active mantle driving component has been

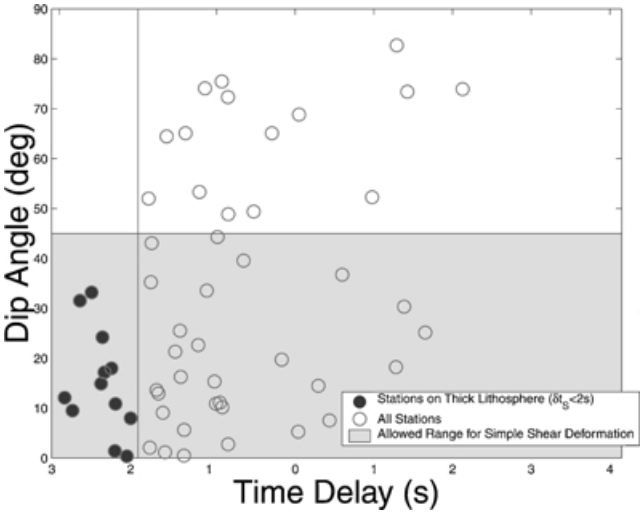

Figure 9. (a) Dip angles of fast axes for stations on the craton (thick lithosphere) ($dt_S < -2$ s) and on slower mantle. Anisotropy due to simple-shear deformation of the lithosphere cannot produce dip angles larger than 45° (see text).

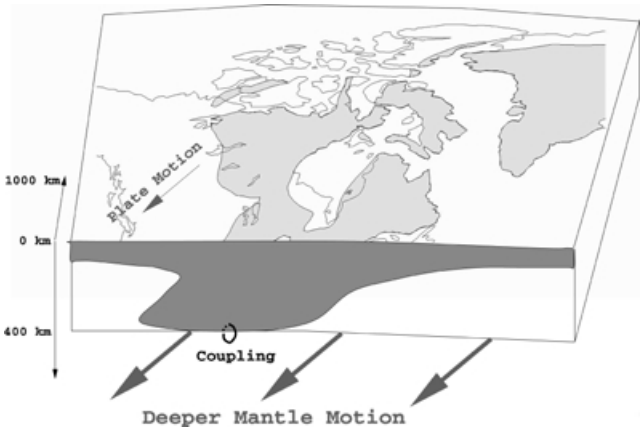

Figure 10. Simple-shear deformation of the thick lithospheric root under the craton due to relative motion with the deeper mantle (illustration). Olivine a-axes dipping to the Southwest (shown schematically) indicate that mantle flow under the craton is in the same direction and faster than the motion of surface plate.

suggested for other continents (Alvarez 1982; Pavoni 1992; Ziegler 1992; Stoddard & Abbott 1996).

7 DISCUSSION

How do these inferences relate to the recent suggestion of a two-layered lithosphere under the Canadian Shield (Bokelmann & Silver 2000) and other regions (Savage & Silver 1993; Levin *et al.* 1999). For the Canadian Shield, *P*- and *S*-station delays were analyzed previously. Together with the shear-wave splitting (Bokelmann & Silver 2000) they require a two-layer anisotropic model in the area with subhorizontal foliation orientation in the deeper layer. This is consistent with results from surface waves (Babuska *et al.* 1998). For the shallower layer a subvertical foliation produced a slightly better fit. With the data in the current study two anisotropic layers cannot be resolved, since the ray paths in the upper mantle are nearly straight ($v_P \approx$ const.). Two layers then produce delay times

$$dt = -\int_{L_1} \frac{\delta v}{v_P^2}\, ds - \int_{L_2} \frac{\delta v}{v_P^2}\, ds \approx -\frac{1}{v_P^2}\left[L_1 \delta\Gamma^1_{ijkl} + L_2 \delta\Gamma^2_{ijkl}\right]\hat{x}_i\hat{x}_j\hat{x}_k\hat{x}_l \quad (18)$$

and the effect of two layers on traveltimes is identical to that of a single layer with elastic constants

$$\delta\Gamma^3_{ijkl} = \frac{L_1 \delta\Gamma^1_{ijkl} + L_2 \delta\Gamma^2_{ijkl}}{L_1 + L_2}. \quad (19)$$

This is for the case of two spherical shells around the station. In the case of two layers, L_1, and L_2 (L_i) must be replaced by $L_i^2/|\hat{x}_3|$, but for teleseismic incidence angles the difference is not large. Assuming that indeed the shallower layer has subvertical and the deeper layer has subhorizontal foliation we may test which layer dominates the anisotropy by testing whether the slow direction is more closely horizontal or subvertical. We do this by computing the scalar product of slow directions, $h = (\hat{\mathbf{e}}_h \cdot \hat{\mathbf{e}}_{slow})$ and $v = (\hat{\mathbf{e}}_v \cdot \hat{\mathbf{e}}_{slow})$ with the horizontal direction $\hat{\mathbf{e}}_h$ and the subvertical direction $\hat{\mathbf{e}}_v$, for each station. $\hat{\mathbf{e}}_h$ and $\hat{\mathbf{e}}_v$ are obtained as the directions orthogonal to the fast direction of the composite data set (which comprises all data on the craton). That fast direction has an azimuth of $\theta = 214°$ and an incidence angle of $\phi = 69°$ from the vertical (dip angle 21°). We obtain mean values $\bar{h} = 0.59$ and $\bar{v} = 0.67$ from the set of stations on the craton, which suggests a roughly equal strength of the anisotropy in both layers. We assumed that the anisotropy in both layers is like that of pure olivine. Other authors have assumed that b- and c-axes of the olivine grains form a girdle around the a-axis. In that case seismology does not help to distinguish the foliation orientation.

The inversions for the stations on the craton suggest that a large part of the delay data are explained by anisotropy. On the craton the anisotropy is consistent with that of a simple-shear deformation. But off the craton 15 stations showed more steeply dipping fast axes suggesting either anisotropy from a more complicated type of deformation or an effect of heterogeneity on the data. Closer inspection of Fig. 5 shows that many of the steeply dipping fast axes occur under stations located near the edge of the craton, where we may expect strong effects from lateral heterogeneity. Such nearby heterogeneity may have an effect on the inversions since it occurs over a potentially large angular region. Conversely, distant heterogeneity, e.g., from the lower mantle would affect only a small part of the lower hemisphere and is therefore not likely to influence the results much. Fig. 11 tests the effect of both anisotropy and lateral heterogeneity on the fast azimuths. Fast directions on the thick lithosphere (a) show good correlation with absolute plate motion (relative to the fixed-hotspot frame,Gordon & Jurdy 1986). There is a small offset however (20°) arising mostly from stations in the far north. The offset is larger and apparent for most stations on the shield if we use a 'no-net-rotation' reference frame, e.g. NNR-NUVEL-1A (DeMets *et al.* 1994). A similar correlation between absolute plate motion and fast directions is not apparent for stations off the craton. But there is a correlation with the direction toward the centre of the craton (d) taken as lat. 58° and long. −83° although with large variance. This is probably due to a laterally heterogeneity velocity structure with a faster mantle under the craton compared with the region around it. There is no hint of such an effect from lateral heterogeneity for stations on the craton. This is an additional indication that fast axes in the region of the craton are not influenced by lateral heterogeneity, while it may have considerable effect in other

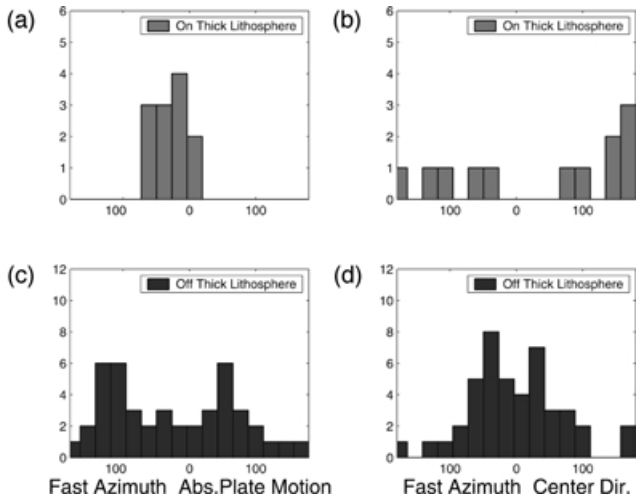

Figure 11. Test of the effect of deep-seated lateral heterogeneity associated with the craton (thick lithosphere) and of anisotropy. Fast directions are displayed relative to the absolute plate motion (a and c) and relative to the direction toward the centre of craton (b and d). Note that fast directions on the craton (a and c) agree well with absolute plate motion directions (and anisotropy due to plate-mantle interaction) whereas fast directions off the craton show a correlation with the direction toward the craton centre but not with absolute plate motion suggesting an effect of lateral heterogeneity there, although the variance is large (see text).

regions. Another factor which may influence fast directions off the craton is the perturbation of mantle flow due to the thick lithospheric root itself. Fouch *et al.* (2000) suggested that this effect explains some of the anisotropic fast azimuths observed off the region of thick root.

On the craton there is a good correlation between fast azimuths from *P*-waves (this study) and SKS-waves (Silver 1996) which supports this study. More importantly even, the western dip of fast axes in the Eastern US has also been observed and thus confirmed by SKS studies in the Appalachian region (Levin *et al.* 1999). Determinations of the fast axis dip from shear-wave splitting are very rare so far. Other studies of that type were done in California (Hartog & Schwartz 2000, 2001). They find that fast axes in Eastern California also have an eastward dip, like an an earlier study of *P*-wave delays that found early *P*-wave residuals from the east in that region (Babuska *et al.* 1993). This is all in agreement with this study, which finds that fast directions in the western US are nearly opposite to the plate motion direction (Fig. 5). This may be caused by simple shear deformation with the opposite sense, which would be reasonable in light of larger-scale mantle convection.

8 CONCLUSIONS

We have given a technique for analyzing teleseismic *P*-wave delays arising from anisotropy along the ray paths. Application to the Canadian Shield and surrounding areas has resulted in a coherent pattern of anisotropy associated with the lithosphere/asthenosphere system in the region of the craton, which underlies large parts of North America. With fast axes dip angles shallower than 45° the type of anisotropy is consistent with simple-shear deformation arising from a mechanical interaction between the lithospheric plate and the underlying mantle. The azimuths of the fast axes imply a southwestward relative motion of the deeper mantle relative to North America, in the direction of absolute plate motion. If this interpretation is correct, it suggests that the mantle helps to drive the plate motion and that the mantle motion is roughly parallel to and faster than the plate motion. Such an active driving component from the mantle has been suggested before by a number of authors (Alvarez 1982; Pavoni 1992; Ziegler 1992; Stoddard & Abbott 1996; Bird 1998), but so far there has not been much geophysical evidence, which strongly requires such a mechanism. An active role of the mantle in driving the plates would however help to explain several tectonic enigmas, e.g. why mountain building is far more frequent on the western side of the Americas than on the eastern side and why the westward motion of North America slowed down dramatically throughout the last 100 million years.

ACKNOWLEDGMENTS

We thank Rob van der Hilst and Hravnkell Kárason for supplying the relocated traveltime data set, and Norman Sleep, Mark Zoback, Simon Klemperer, Paul Silver and Peter Bird for discussions. Reviews of Michael Korn, Martha Savage, and an anonymous reviewer improved the manuscript. The author is grateful to the Deutsche Forschungsgemeinschaft (DFG) for support.

REFERENCES

Alvarez, W., 1982. Geological evidence for the geographical pattern of mantle return flow and the driving mechanism of plate tectonics, *J. geophys. Res.,* **87,** 6697–6710.

Babuska, V., Plomerova, J. & Sileny, J., 1993. Models of seismic anisotropy in the deep continental lithosphere, *Phys. Earth planet. Int.,* **78,** 167–191.

Babuska, V., Montagner, J.P., Plomerova, J. & Girardin, N., 1998. Age-dependent large-scale fabric of the mantle lithosphere as derived from surface-wave velocity anisotropy, in *Geodynamics of lithosphere and Earth's mantle; seismic anisotropy as a record of the past and present dynamic processes,* eds Liebermann, R.C. & Babuska, V., *Pure appl. Geophys.,* **151,** 257–280.

Backus, G., 1965. Possible forms of seismic anisotropy of the uppermost mantle under oceans, *J. geophys. Res.,* **70,** 3429–3439.

Backus, G., 1970. A geometrical picture of anisotropic elastic tensors, *Rev. Geoph. Sp. Phys.,* **8,** 633–671.

Bird, P., 1998. Testing hypotheses on plate-driving mechanisms with global lithosphere models including topography, thermal structure, and faults, *J. geophys. Res.,* **103,** 10 115–10 129.

Bokelmann, G.H.R. & Silver, P.G., 2000. Mantle variation within the Canadian Shield: Traveltimes from the APT89 portable broadband transect, *J. geophys. Res.,* **105,** 579–605.

Courant, R. & Hilbert, D., 1924. *Methoden der mathematischen Physik,* Springer-Verlag, Berlin.

DeMets, C., Gordon, R.G., Argus, D.F. & Stein, S., 1994. Effect of recent revisions to the geomagnetic reversal timescale on estimates of current plate motions, *Geophys. Res. Lett.,* **21,** 2191–2194.

Dziewonski, A.M. & Anderson, D.L., 1981. Preliminary reference Earth model (PREM), *Phys. Earth planet. Int.,* **25,** 297–356.

Engdahl, E.R., van der Hilst, R. & Buland, H., 1998. Global teleseismic earthquake relocation with improved traveltimes and procedures for depth determination, *Bull. seism. Soc. Am.,* **88,** 722–743.

Fouch, M.J., Fischer, K.M., Parmentier, E.M., Wysession, M.E. & Clarke, T.J., 2000. Shear wave splitting, continental keels, and patterns of mantle flow, *J. geophys. Res.,* **105,** 6255–6276.

Gordon, R.G. & Jurdy, D.M., 1986. Cenozoic global plate motions, *J. geophys. Res.,* **91,** 12 389–12 406.

Grand, S.P., 1994. Mantle shear structure beneath the Americas and surrounding oceans, *J. geophys. Res.,* **99,** 11 591–11 621.

Hartog, R. & Schwartz, S.Y., 2000. Subduction-induced strain in the upper mantle east of the Mendocino triple junction, California, *J. geophys. Res.,* **104,** 7909–7930.

Hartog, R. & Schwartz, S.Y., 2001. Depth-dependent mantle anisotropy below the San Andreas fault system: Apparent splitting parameters and waveforms, *J. geophys. Res.,* **106,** 4155–4167.

Hess, H.H., 1964. Seismic anisotropy of the uppermost mantle under oceans, *Nature,* **203,** 629–631.

Kárason, H. &Van der Hilst, R.D., 2001. Tomographic imaging of the lowermost mantle with differential times of refracted and diffracted core phases (PKP, Pdiff), *J. geophys. Res.,* **106,** 6569–6588.

Kennett, B.L.N., Engdahl, E.R. & Buland, R., 1995. Constraints on seismic velocities in the Earth from traveltimes, *Geophys. J. Int.,* **122,** 108–124.

Kumazawa, M. & Anderson, O.I., 1969. Elastic moduli, pressure derivatives, and temperature derivatives of single-crystal olivine and single-crystal forsterite, *J. geophys. Res.,***74,** 5961–5972.

Larson, K.M., Freymueller, J. & Philipsen, S., 1997. Global Plate Velocities from the Global Positioning System, *J. geophys. Res.,* **102,** 9961–9982.

Levin, V., Menke, W. & Park, J., 1999. Shear wave splitting in the Appalachians and the Urals: A case for multilayered anisotropy, *J. geophys. Res.,* **104,** 17 975–17 993.

Mochizuki, E., 1995. Anisotropic tomography of *P*-wave traveltimes, *Geophys. J. Int.,* **123,** 297–300.

Montagner, J.P., 1996. Surface waves on a global scale; influence of anisotropy and anelasticity, in *Seismic modelling of Earth structure,* eds Boschi, E., Ekstrom, G. & Morelli, A., 81–148, Editrice Compositori, Bologna.

Nicolas, A. & Christensen, N.I., 1987. Formation of anisotropy in upper mantle peridotites—A review, in *Composition, Structure and Dynamics of the Lithosphere-Asthenosphere System,* ed. Fuchs, K., *Geodyn. Ser.,* **16,** 111–123, AGU, Washington, DC.

Nolet, G., 1987. Seismic wave propagation and seismic tomography, 1-23, in *Seismic Tomography,* eds Nolet, G. & Reidel, D., Publ. Co.

Pavoni, N., 1992. Rifting of Africa and pattern of mantle convection beneath the African plate, *Tectonophysics,* **215,** 35–53.

Polet, J. & Anderson, D.L., 1993. Depth extent of cratons as inferred from tomographic studies, *Geology,* **23,** 205–208.

Pollack, H.N., Hurter, S.J. & Johnson, J.R., 1993. Heat flow from the Earth's interior; analysis of the global data set, *Rev. Geophys.,* **31,** 267–280.

Press, W.H., Flannery, B.P., Teckolsky, S.A. & Vetterling, W.T., 1986. *Numerical Recipes: The Art of Scientific Computing,* Cambridge University Press, Cambridge.

Riedesel, M.A. & Jordan, T.H., 1989. Display and assessment of seismic moment tensors, *Bull. seism. Soc. Am.,* **79,** 85–100.

Savage, M.K. & Silver, P.G., 1993. Mantle deformation and tectonics: constraints from seismic anisotropy in the western United States, *Phys. Earth planet. Int.,* **78,** 207–227.

Sayers, C.M., 1994. *P*-wave propagation in weakly anisotropic media, *Geophys. J. Int.,* **116,** 799–805.

Silver, P.G., 1996. Seismic anisotropy beneath the continents: Probing the depths of geology, *Annu. Rev. Earth Planet. Sci.,* **24,** 385–432.

Silver, P.G. & Chan, W.W., 1991. Shear wave splitting and subcontinental mantle deformation, *J. geophys. Res.,* **96,** 16 429–16 454.

Silver, P.G. & Jordan, T.H., 1982. Optimal estimation of scalar seismic moment, *Geophys. J. R. astr. Soc.,* **70,** 755–787.

Smith, M.L. & Dahlen, F.A., 1973. The azimuthal dependence of Love and Rayleigh wave propagation in a slightly anisotropic medium, *J. geophys. Res.,* **78,** 3321–3333.

Stoddard, P.R. & Abbott, D., 1996. Influence of the tectosphere upon plate motion, *J. geophys. Res.,* **101,** 5425–5433.

Vinnik, L.P., Makeyeva, L.I., Milev, A. & Usenko, A. Yu., 1992. Global patterns of azimuthal anisotropy and deformations in the continental mantle, *Geophys. J. Int.,* **111,** 433–447.

Wenk, H.-R., Bennett, K., Canova, G.R. & Molinari, A., 1991. Modeling plastic deformation of peridotite with the self-consistent theory, *J. geophys. Res.,* **96,** 8337–8349.

Zhang, Y.-S. & Tanimoto, T., 1990. Global Love wave phase velocity variation and its significance to plate tectonics, *Phys. Earth planet. Int.,* **66,** 160–202.

Ziegler, P., 1992. Plate tectonics, plate moving mechanisms and rifting, *Tectonophysics,* **215,** 9–34.

APPENDIX A: ANGULAR VELOCITY VARIATION

For weak anisotropy, $\delta v(\theta, \phi)$ may be expanded into spherical harmonics

$$\delta v(\theta, \phi) = \sum_{l=0}^{4} \sum_{m=-l}^{l} R_{lm} P_l^m(\phi) e^{-im\theta} \tag{A1}$$

with complex coefficients $R_{lm} = \alpha_{lm} + i\beta_{lm}$ (Sayers 1994) and normalized associated Legendre polynomials $P_l^m(\phi)$. To ensure a real δv we must have

$$\alpha_{l\bar{m}} = \alpha_{lm}, \qquad \beta_{l\bar{m}} = -\beta_{lm} \tag{A2}$$

for $\bar{m} = -m$. From the symmetry of the spherical harmonic

$$Y_{l\bar{m}}(\theta, \phi) = (-1)^m Y_{lm}^*(\theta, \phi) \tag{A3}$$

and

$$Y_{lm}(\theta, \phi) = (-1)^m \sqrt{\frac{2l+1}{4} \frac{(l-m)!}{(l+m)!}} P_l^m(\phi) e^{-im\theta} \tag{A4}$$

we obtain the symmetry of the normalized associated Legendre function

$$P_l^{-m}(\phi) = (-1)^m \frac{(l-m)!}{(l+m)!} P_l^m(\phi) \tag{A5}$$

With Legendre polynomials in the form

$$\begin{aligned}
P_0^0 &= 1 \\
P_2^0 &= \frac{3}{4}\cos 2\phi + \frac{1}{4} \\
P_2^1 &= -\frac{3}{2}\sin 2\phi \\
P_2^2 &= -\frac{3}{2}\cos 2\phi + \frac{3}{2} \\
P_4^0 &= \frac{35}{64}\cos 4\phi + \frac{5}{16}\cos 2\phi + \frac{9}{64} \\
P_4^1 &= -\frac{35}{16}\sin 4\phi - \frac{5}{8}\sin 2\phi \\
P_4^2 &= -\frac{105}{16}\cos 4\phi + \frac{15}{4}\cos 2\phi + \frac{45}{16} \\
P_4^3 &= -\frac{105}{8}\sin 4\phi + \frac{105}{4}\sin 2\phi \\
P_4^4 &= \frac{105}{8}\cos 4\phi - \frac{105}{2}\cos 2\phi + \frac{315}{8}
\end{aligned}$$

we obtain an angular variation in the form of a Fourier series

$$\begin{aligned}
\delta v(\theta, \phi) = {} & A + B\cos 2\phi + C\cos 2\theta + D\sin 2\theta + E\cos 4\theta \\
& + F\sin 4\theta + G\sin 2\phi\cos\theta + H\sin 2\phi\sin\theta \\
& + J\cos 2\phi\cos 2\theta + K\cos 2\phi\sin 2\theta + L\sin 2\phi\cos 3\theta \\
& + M\sin 2\phi\sin 3\theta + N\cos 2\phi\cos 4\theta + O\cos 2\phi\sin 4\theta \\
& + P\sin 4\phi\cos\theta + Q\sin 4\phi\sin\theta + R\sin 4\phi\cos 3\theta \\
& + S\sin 4\phi\sin 3\theta + T\cos 4\phi\cos 2\theta + U\cos 4\phi\sin 2\theta \\
& + V\cos 4\phi\cos 4\theta + W\cos 4\phi\sin 4\theta
\end{aligned} \tag{A6}$$

Ignoring terms of order and/or degree higher than 2 gives eq. (8). The coefficients A-W can be related to elastic coefficients using expressions in Smith & Dahlen (1973) and Sayers (1994).

APPENDIX B: ERROR CONTOURS

It is customary to search for a solution which minimizes

$$\chi^2 = |(\mathbf{d} - \mathbf{Am})/\sigma|^2, \tag{B1}$$

and which has the smallest length in the nullspace. This is achieved by using the singular value decomposition $\mathbf{A} = \mathbf{U}\Lambda\mathbf{V}^T$ (Press *et al.* 1986) which produces the solution

$$\tilde{\mathbf{m}} = \mathbf{V}\Omega\mathbf{U}^T\mathbf{d} \tag{B2}$$

with the diagonal matrix $\mathbf{\Omega}$ containing the inverses of the nonzero singular values of $\mathbf{A}$ (from the diagonal of $\mathbf{\Lambda}$). The covariance matrix of $\mathbf{m}$ is

$$\mathbf{C_m} = \left\langle (\mathbf{m} - \mathbf{m}_0)(\mathbf{m} - \mathbf{m}_0)^T \right\rangle = \sigma^2 \mathbf{V\Pi V}^T \tag{B3}$$

with $\mathbf{\Pi} = \mathbf{\Omega}{:}\mathbf{\Omega}$, $\mathbf{m}_0 = \langle \mathbf{m} \rangle$, and the *a priori* data error σ, here assumed constant. More realistically, σ is replaced by the *a posteriori* error $\sigma' = \sqrt{\chi^2/(N-p)}\sigma$. p is the number of model parameters to be estimated.

Errors of the velocities δl_1, δl_2, and δl_3 and the axis orientations $\delta\hat{\mathbf{e}}_1$, $\delta\hat{\mathbf{e}}_2$, $\delta\hat{\mathbf{e}}_3$ can be obtained from perturbation theory (Courant & Hilbert 1924; Riedesel & Jordan 1989). We follow Riedesel & Jordan (1989) and define a vector

$$\mathbf{g} = (G_{11}, G_{22}, G_{33}, \sqrt{2}G_{12}, \sqrt{2}G_{13}, \sqrt{2}G_{23})^T. \tag{B4}$$

The isomorphism $\mathbf{g} \Leftrightarrow \mathbf{G}$ preserves the Euklidean norm, that is $\mathbf{g} \cdot \mathbf{g} = \mathbf{G} : \mathbf{G}$. This allows a compact representation of the fourth-order covariance matrix of $\mathbf{G}$ through a second-order matrix $\mathbf{C}_{\hat{\mathbf{g}}}$ in terms of the normalized vector $\hat{\mathbf{g}} = \mathbf{g}/\sqrt{\mathbf{g} \cdot \mathbf{g}}$. The projection onto the tangent plane can be written to first order as

$$\mathbf{C}_{\hat{\mathbf{g}}} = \frac{1}{\mathbf{g} \cdot \mathbf{g}} \left(\mathbf{I} - \hat{\mathbf{g}}_0 \hat{\mathbf{g}}_0^T\right) \cdot \mathbf{C}_{\mathbf{g}} \cdot \left(\mathbf{I} - \hat{\mathbf{g}}_0 \hat{\mathbf{g}}_0^T\right) \tag{B5}$$

(Silver & Jordan 1982) with $\hat{\mathbf{g}}_0 = \langle \hat{\mathbf{g}} \rangle$ and $\mathbf{C}_{\mathbf{g}} = \langle (\mathbf{g} - \mathbf{g}_0)(\mathbf{g} - \mathbf{g}_0)^T \rangle$. To first order, the perturbation of the eigenvector $\delta\hat{\mathbf{e}}_i$ is orthogonal to the eigenvector. The perturbation of the eigenvalue δl_i can be written as

$$\delta l_i = \delta\hat{\mathbf{g}} \cdot \hat{\mathbf{n}}_{ii}. \tag{B6}$$

with the vector $\mathbf{n}_{ij} \Leftrightarrow \mathbf{N}_{ij} = \hat{\mathbf{e}}_i \hat{\mathbf{e}}_j$. Then we can write the covariance of the eigenvalues (velocities) as

$$[\mathbf{C}_l]_{ij} = \langle \delta l_i \delta l_j \rangle = \hat{\mathbf{n}}_{ii} \cdot \mathbf{C}_{\hat{\mathbf{g}}} \cdot \hat{\mathbf{n}}_{jj} \tag{B7}$$

The first-order perturbation of the i-th eigenvector is

$$\delta\hat{\mathbf{e}}_i = \sum_{i \neq n} \delta\hat{\mathbf{g}} \cdot \frac{\hat{\mathbf{n}}_{ni}}{l_n - l_i} \hat{\mathbf{e}}_i. \tag{B8}$$

(Courant & Hilbert 1924). This leads to the covariance matrix for the i-th eigenvector

$$\mathbf{C}_{\hat{\mathbf{e}}} = \langle \delta\hat{\mathbf{e}}_i \delta\hat{\mathbf{e}}_i \rangle = \sum_{m \neq i} \sum_{l \neq i} \frac{\hat{\mathbf{n}}_{mi}}{l_i - l_m} \cdot \mathbf{C}_{\hat{\mathbf{g}}} \cdot \frac{\hat{\mathbf{n}}_{li}}{l_i - l_l} \hat{\mathbf{N}}_{ml}. \tag{B9}$$

From the covariance matrix $\mathbf{C}_{\hat{\mathbf{e}}}$ the ellipsoidal confidence regions for the fast, intermediate, and slow axes can be constructed and displayed on the lower hemisphere. These confidence regions don't include trade-offs between the different axes, and are therefore somewhat optimistic.